Short-Term Solar Irradiance Forecasting via Satellite/Model Coupling

Steven D. Miller[1], Matthew A. Rogers[1], John M. Haynes[1], Manajit Sengupta[2], and Andrew K. Heidinger[3]

[1]Cooperative Institute for Research in the Atmosphere, Colorado State University, Ft. Collins, CO

[2]National Renewable Energy Laboratory, Golden, CO

[3]National Oceanic and Atmospheric Administration, National Environmental, Satellite, and Data Information Service, Advanced Satellite Products Branch, Madison, WI

An Invited Review Paper Submitted to *Progress in Solar Energy*

Special Issue (Jan Kleissl, Editor)

8 November 2017

Corresponding Author:

Steven D. Miller (Steven.Miller@colostate.edu)

970.491.8037

Abstract

The short-term (0-3 hr) prediction of solar insolation for renewable energy production is a problem well-suited to satellite-based techniques. The spatial, spectral, temporal and radiometric resolution of instrumentation hosted on the geostationary platform allows these satellites to describe the current cloud spatial distribution and optical properties. These properties relate directly to the transient properties of the downwelling solar irradiance at the surface, which come in the form of 'ramps' that pose a central challenge to energy load balancing in a spatially distributed network of solar farms. The short-term evolution of the cloud field may be approximated to first order simply as translational, but care must be taken in how the advection is handled and where the impacts are assigned. In this research, we describe how geostationary satellite observations are used with operational cloud masking and retrieval algorithms, wind field data from numerical weather prediction (NWP), and radiative transfer calculations to produce short-term forecasts of solar insolation for applications in solar power generation. The scheme utilizes retrieved cloud properties to group pixels into contiguous cloud objects whose future positions are predicted using four-dimensional (space + time) model wind fields, selecting steering levels corresponding to the cloud height properties of each cloud group. The shadows associated with these clouds are adjusted for sensor viewing parallax displacement and combined with solar geometry and terrain height to determine the actual location of cloud shadows. For mid/high-level clouds at mid-latitudes and high solar zenith angles, the combined displacements from these geometric considerations are non-negligible. The cloud information is used to initialize a radiative transfer model that computes the direct and diffuse-sky solar insolation at both shadow locations and intervening clear-sky regions. Here, we describe the formulation of the algorithm and validate its performance against Surface Radiation (SURFRAD; Augustine et al., 2000, 2005) network observations. Typical errors range from 8.5% to 17.2% depending on the complexity of cloud regimes, and an operational demonstration outperformed persistence-based forecasting of Global Horizontal Irradiance (GHI) under all conditions by ~10 W/m^2.

Keywords: Geostationary Satellite, Cloud Properties, Parallax, Shadows, Advection, Solar Irradiance

1. Introduction

Ephemeral cloud cover (e.g., fair-weather cumulus fields) presents a key challenge to the generation of power using photovoltaic (PV) and concentrated solar power (CSP) systems distributed worldwide. Cloud shadows reduce the direct beam solar irradiance significantly and modulate the diffuse-sky radiation distribution as well, impacting the overall global horizontal irradiance (GHI) available for renewable energy production. The rapid, high-amplitude fluctuations to the available solar energy at the surface that result from shadow passage are referred to in the power and energy industry as 'ramps.' These ramps have a marked impact on power generation efficiency at multiple space and time scales (Perez et al., 2016).

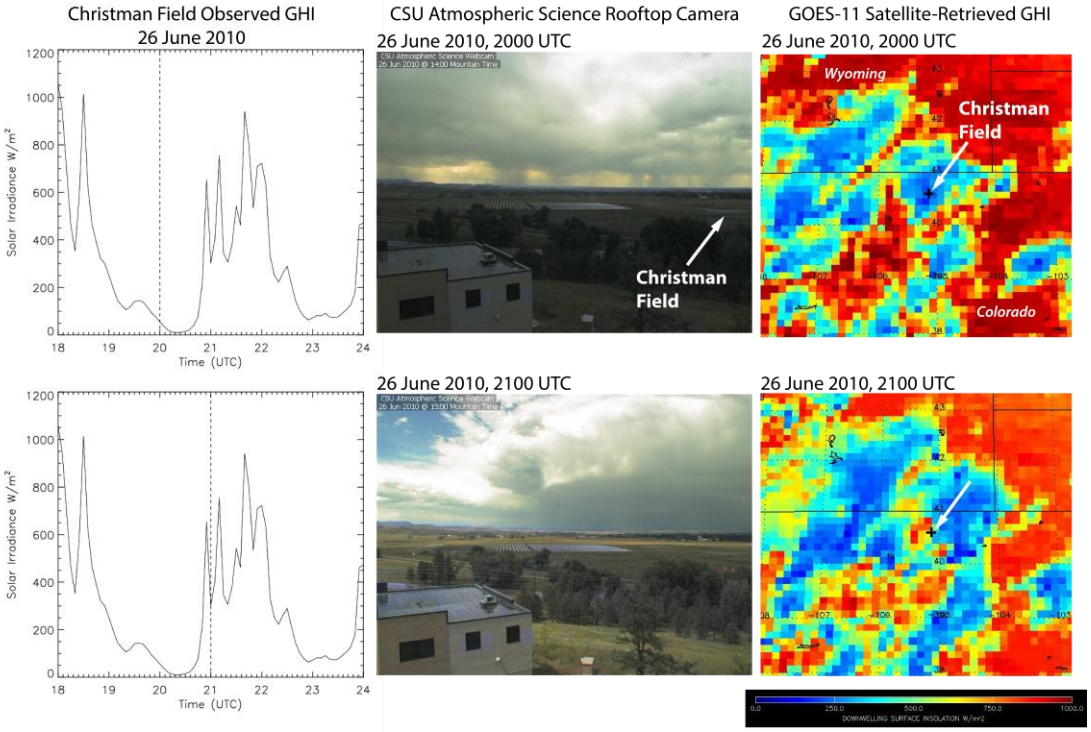

Fig. 1. Example of a solar irradiance ramping event as measured from the surface and satellite for a case at Christman Field, Ft. Collins, CO on 26 June 2017 at 2000 UTC (top row) and 2100 UTC (bottom row). The left, center, and right columns show (respectively) i) time-matched global horizontal irradiance (GHI) from a pyranometer located at Christman Field, Ft. Collins, CO (vertical dashed lines denote the 2000 and 2100 UTC times corresponding to the photos and satellite data), ii) observations from a north/northwest (335° azimuth, 64° field of view) viewing rooftop camera, and iii) GOES-11 satellite-retrieved estimates of GHI (blue regions correspond to thick clouds, orange/red regions correspond to clear-sky, and the location of Christman Field denoted by white arrow).

The high variability of the solar resource, caused principally by ramps of various strength and intervals, are tied to the macro- and microphysical properties of the intervening cloud cover. A surface/satellite perspective on broken cumulus clouds, most often associated with complex ramping behavior, is shown for an example over the Colorado Front Range in Fig. 1. In this case, an approximately 700 W/m^2 increase (upward ramp) of solar irradiance corresponds to a break in the

optically thick, broken cloud cover formed by sporadic afternoon thunderstorms. The solar radiation subsequently drops by a similar amount as a downward ramp upon the arrival of shadows from clouds to the southwest.

Optimal integration of PV and CSP systems into a power grid requires advanced knowledge of both the general likelihood and specific timing of ramps. Accurate ramp prediction requires in turn an accuracy in identifying and predicting the motion of clouds, and specifically the locations and magnitude of their shadows. Addressing this need both probabilistically and deterministically in the short-term forecast time horizon (e.g., 0-7 hr) provides solar energy suppliers with information critical in supporting decisions on load balancing and transmission switching in a spatially distributed network, dispatching energy at optimal times, and facilitating the overall penetration of solar power on the electric grid.

There exist several methods for forecasting cloud impacts to solar energy (referred to here as radiation falling between the wavelength range of 290 nm to 3 μm, which accounts for ~97% of the total energy; Sengupta et al., 2015), each optimized to a specific spatial and temporal scale (Diagne et al., 2013). Observational techniques at short time windows are better suited to describing the current distribution of clouds and cloud properties deterministically, leading to better short-term forecasts of ramps predicated on the continuity and simple advection of this field. At temporal scales of 0-0.5 hr, information from persistence (Lee et al., 2017), giving way to surface-based all-sky camera networks (Kleissl et al., 2010; Chow et al. 2011), provide the most accurate predictive capability. At intra-day forecast timeframes of ~0.5-3 hr, airborne or satellite-based platforms provide a useful description of clouds that reside beyond the local horizon view of surface-based networks. The skill associated with forecasting simple (non-evolving) cloud field advection via observed or model-supplied motion vectors depends on the cloud type and meteorological regime. At multi-hour to day-ahead timeframes, observation-based methods give way in skill to numerical weather prediction (NWP) based systems (Inman et al., 2013). At these longer time horizons, the cloud field is best described by atmospheric dynamics and thermodynamics which drive cloud formation, dissipation, and cloud microphysical evolution rather than advection of the initially observed cloud field.

Environmental satellites have measured solar energy reflected from the earth/atmosphere system for many decades (Vonder Haar et al., 1973), and satellite-based methods for solar energy forecasting and resource assessment are now very well established (Miller et al., 2013). Empirical methods (e.g., Tarpley, 1979; Cano et al., 1986; Schmetz, 1989; Perez et al., 2002) relate satellite observations of cloud reflectance to atmospheric transmittance. Specifically, ground-based measurements of the minimum and maximum observed GHI are related linearly to a normalized cloud index derived from the satellite reflectance data. Physical methods (e.g., Gautier et al., 1980; Diak and Gautier, 1983; Dedieu et al., 1987; Darnell et al., 1988) enlist radiative transfer modeling to retrieve the surface radiation field directly from the satellite observations. Typical RMSE for satellite-based global hourly radiation assessment is 17-25% (Polo et al, 2008). The main sources of error reside in microscale variability of the radiation field, caused by cloud shadows (Zelenka et al., 1999).

The focus of this paper is on improving satellite-based solar forecasting techniques of cloud-induced solar energy ramps over time scales that help to bridge the gap in capabilities between the near-casting (persistence and all-sky camera systems) and forecasting (NWP) regimes. As mentioned above, determination of the mesoscale cloud distribution and tracking its motion via advection techniques is tailored to the 0.5-3 hr forecast window. Here, we describe results of a cloud advection scheme that is applicable to current and future geostationary satellite observations. Referred to hereafter as the Cooperative Institute for Research in the Atmosphere's (CIRA) solar forecasting system, or *CIRACast*, the prediction scheme leverages cloud properties from operational quantitative algorithms, four-dimensional steering winds from NWP model (which assimilates rawinsonde and satellite-derived winds), and a radiative transfer code to compute surface radiation values of advected cloud systems. As an advance to the current state of the art, and in anticipation of high space/time resolution geostationary systems, we consider cloud shadow locations that have been geometrically-adjusted for viewer parallax and the solar geometry using satellite estimates of cloud height.

The paper is structured as follows. Section 2 provides an overview of the satellite-retrieved cloud properties, numerical model data, and radiative transfer components of *CIRACast*. Section 3 details the methodology of coupling these components to address the short-term prediction problem, including the satellite-specific geometric considerations for proper cloud shadow location assignment. Examples of performance, sensitivity, caveats of the method, and its performance incorporated within an operational multi-scale solar forecasting system are presented in Section 4. Section 5 considers the outstanding and emergent needs for improved solar forecasting tools, and outlines how the next generation of geostationary environmental satellites can help to address them. Section 6 summarizes the paper and looks toward future development. Appendix A provides details on the calculations used for parallax and shadow casting.

2. Observational and Model Datasets

CIRACast is a fusion of three main elements: 1) cloud macro- and microphysical properties derived from satellite observations, 2) short-term NWP model wind fields, and 3) a radiative transfer model relating the space/time evolving field of clouds to the surface downwelling solar irradiance. This downwelling irradiance is composed of the direct normal irradiance (DNI) and diffuse horizontal irradiance (DHI), which together form the Global Horizontal Irradiance (GHI):

(1)

where θ_{sun} is the local solar zenith angle. GHI is the parameter of interest to PV arrays, while DNI is the more relevant parameter for CSP sites. Whereas atmospheric aerosol plays an important role for DNI, it plays a lesser role in ramp-induced changes to the GHI (apart from extreme cases, e.g., near smoke/dust plumes or along frontal boundaries). As such, the focus of this work is on cloud-induced ramps. This section introduces the three main elements of *CIRACast*, followed in Section 3 by an explanation of how they are coupled.

2.1 Satellite-Based Cloud Property Retrievals

The Clouds from the Advanced Very High Resolution Radiometer (AVHRR)–Extended (CLAVR-x; Heidinger et al., 2009; Heidinger et al., 2010; Heidinger 2012; Pavolonis et al., 2005; Walther and Heidinger, 2012) is an operational code package (available online at: https://cimss.ssec.wisc.edu/cspp/clavrx_v2.0.shtml) developed by the National Oceanic and Atmospheric Administration (NOAA). Originally designed for AVHRR, as its name implies, CLAVR-x has since been extended to accommodate a variety of similar-class satellite optical spectrum (visible, near-infrared, middle-infrared, and thermal infrared bands) satellite radiometers flying upon various platforms, including geostationary observations from the Geostationary Operational Environmental Satellite (GOES) series and members of the international geostationary constellation (e.g., Meteosat and Himawari).

CLAVR-x derives pixel-scale information on cloud distribution and physical/optical properties, including liquid/ice phase, cloud-top height/pressure, and cloud optical depth and effective particle radius. The daytime cloud mask employs a dark-sky background, based on monthly cloud-cleared composite imagery and an updating ancillary snow cover database. For GOES cloud properties processing at CIRA, the georeferenced cloud properties from CLAVR-x are computed in near real-time based on direct broadcast satellite data, and are distributed immediately upon completion for use in the cloud advection code via automated processing scripts.

2.2 Numerical Weather Prediction Model Data

Whereas CLAVR-x provides an estimate of the instantaneous cloud distribution, useful for solar resource assessments (Sengupta et al., 2015), *CIRACast* predicts how this distribution will evolve in the short-term. It enlists a four-dimensional (space+time) model wind field from a Numerical Weather Prediction (NWP) model to propagate cloud locations forward in time at configurable spatial and temporal resolution. To provide operational relevance, *CIRACast* enlists NOAA's Global Forecast System (GFS) NWP model for this purpose. The GFS provides initialization times of 00, 06, 12, and 18 UTC, and 3-hourly forecast time steps going out 24 hours from each initialization time.

Model winds at all levels from the closest initialization time are interpolated linearly between model time steps bracketing the current satellite image (or forecasted satellite field) time. This interpolation provides an evolving description of the stream function across space and time, including the representation of curvature in the flow not captured by techniques that apply a linear wind vector defined at initialization time. *CIRACast* uses the interpolated wind field to steer clouds based on their CLAVR-x estimated heights. In addition, information on total column ozone and precipitable water are extracted from the GFS fields for use by the standalone radiative transfer code, described below.

2.3 Surface Irradiance Radiative Transfer Calculations

Once the cloud field has been advanced per the interpolated winds, we must determine the surface irradiance at the new cloud shadow locations. The CLAVR-x package contains an embedded version of the Satellite Algorithm for Shortwave Radiation Budget (SASRAB) (Pinker and Laszlo, 1992; Pinker et al., 1995; Pinker et al., 2000) radiative transfer code, used for global radiation

budget studies. However, the solar forecasting problem requires calculations of irradiance for future states. In the initial version of *CIRACast*, a stand-alone version of SASRAB is applied in a forecast mode.

Inputs to SASRAB include cloud properties and visible-band reflectance, precipitable water and ozone, the solar/satellite geometry, and surface reflectance properties. These parameters are saved to the *CIRACast* output grid and used for computing the surface irradiance at each time step. The cloud information comes from CLAVR-x. The solar geometry and viewer parallax (described in Section 3) are updated via geometric calculations. Precipitable water and ozone information, used in the radiative transfer calculations for GHI, comes from the GFS model. The cloud-cleared visible reflectance background required by SASRAB utilizes the same field used by CLAVR-x for its cloud masking. This background uses CONUS-centered composites of the second-darkest GOES visible band reflectance encountered at each pixel, provided for each scan time, in the two-week period. For example, a two-hour satellite forecast, initialized at 16Z and valid at 18Z on the 15th of February would utilize the 18Z cloud-cleared GOES image compiled over the period 1-14 February. The background accounts for the possibility of highly-variable surface properties such as snow cover, which if unaccounted for would masquerade as a false cloud, with associated false surface irradiance impacts (Perez et al., 2002). SASRAB is designed to run on a pixel-by-pixel basis throughout the output grid. It is also possible to apply the code to 3x3 pixel groups of pixels, as a way of imparting smoothness to the radiation field.

3. Methodology

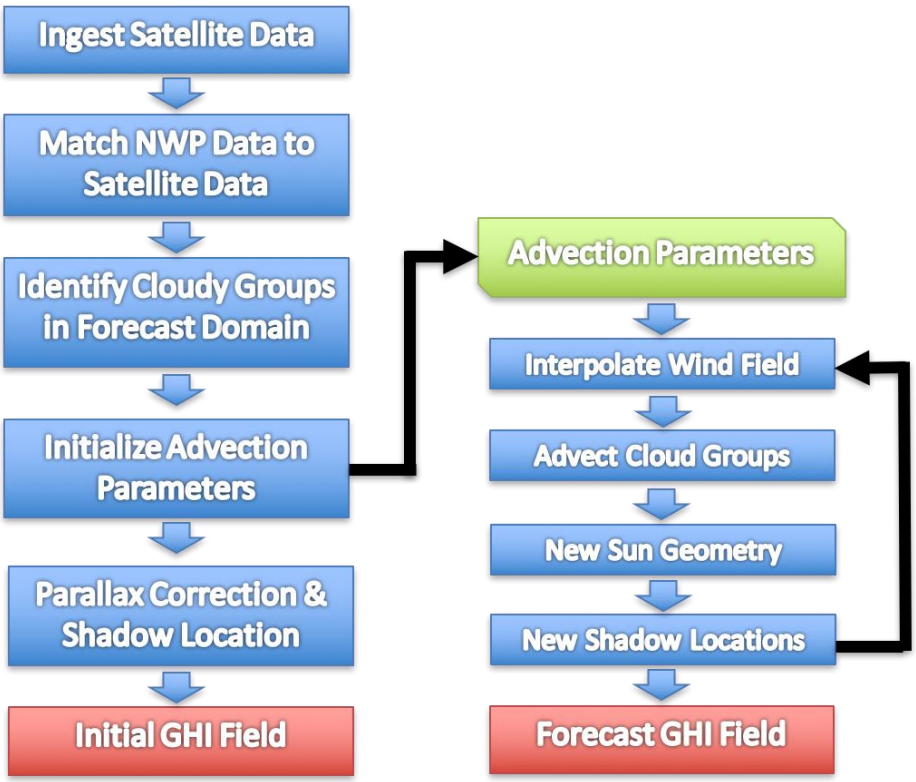

Fig. 2. General flow diagram for CIRACast initialization and short-term forecasts of GHI.

A simple schematic of the processing flow for *CIRACast* is shown in Fig. 2. Beginning with a new satellite image collection, we obtain corresponding NWP model data (analysis or short-term forecast as required to match the satellite image time). CLAVR-x is called to compute the cloud mask, type, and property information for domains of interest. Based on the satellite-identified cloud field, cloud objects are identified using property similarity (discussed below). We then determine the location of cloud shadows based on parallax correction and shadow-casting, and compute an initial-time downwelling solar irradiance at the surface field.

Using interpolated NWP wind information, the cloud groups are then advanced by height-dependent steering winds to their new locations. New shadow locations are computed, and all necessary cloud information needed for SASRAB irradiance calculations are stored in an output grid which has the same spatial dimension as the original domain. The parameters stored are: satellite zenith angle, solar zenith angle, relative satellite/solar azimuth angle, sun glint angle, visible reflectance, cloud mask result, snow fraction, time-interpolated dark-sky background, cloud optical depth, cloud top effective radius, cloud type, cloud top pressure, cloud top height, column ozone, column precipitable water, latitude, longitude, scan time, and cloud water path.

3.1 Assignment of Cloud Objects

Early versions of *CIRACast* considered cloud pixels as independent cloud objects and tracked them individually over space/time. This approach can lead to the break-up of contiguous clouds over time, particularly in the presence of a strongly divergent wind field and at longer forecast times. This led in turn to spurious ramps due to the "clear" gaps formed by the divergence of previously adjacent cloud pixels—an unphysical result. The pixel-level advection is also computationally inefficient—requiring the tracking of potentially thousands of cloudy pixels for even a modest domain size (e.g., a box of dimension several hundred km on a side), depending on the regional cloud coverage.

To mitigate these issues, a modification to the logic was introduced wherein cloudy pixels were associated as contiguous objects or 'groups.' Assignment of groups is based on a weighted score of differences in the cloud properties listed in Table 1; similar cloud pixels (determined by experimentally-determined thresholds of proximity in cloud parameter space) form individual groups while dissimilar pixels form new cloud groups. The scheme first clusters cloud pixels based on their connectivity and then assesses their similarity in retrieved cloud properties via Table 1.

Table 1: Tests, Thresholds, and Weights for adjacent pixel group assignment

Test Parameter	*Threshold Value*	*Weight*
Same cloud type	n/a	0.35
Similar cloud type	n/a	0.25
Change in cloud-top height	3-5 km	0.30
Change in effective radius	5-10 μm	0.05
Change in cloud optical depth	5-10	0.05

The ranges of threshold values in Table 1 apply to different cloud types. For cloud top height, the threshold is 3 km for low/liquid, super-cooled, mixed-phase, cirrus, and overlapping clouds, and 5 km for opaque ice and overshooting tops (deep convection). For effective radius, the threshold is 5 μm for low/liquid and super-cooled clouds, and 10 μm for all other types. For optical depth, the threshold is 10 for mixed-phase and 5 for all other cloud types. Similar rules associate liquid-phase clouds of low/super-cooled/mixed cloud types, and ice-phase clouds of cirrus/opaque ice/overshooting/overlap cloud types. These thresholds were obtained experimentally, but are based on the observed variability in cloud properties and morphology (e.g., Miller et al., 2014).

Looping over the rows (from north to south) and columns (from west to east) of the satellite domain, each pixel is compared against any adjacent pixels that have already been evaluated. For the base case of the first cloudy pixel encountered, a default group identifier number is assigned to it and the next pixel in the loop is considered. The number of previously-evaluated pixels used in group evaluating the current pixel varies per the cloud spatial distribution and the position of the current pixel in the image array. A weighted score of similarity based on the tests, thresholds and weights provided in Table 1, is computed as follows. Each test produces a value between 0.0 and 1.0, depending on the similarity of the current pixel and the adjacent pixel. For example, if the cloud top height for the adjacent pixel is identical to the current pixel cloud top height, a value of 1.0

is assigned for that adjacent pixel location, but if the adjacent pixel cloud top height deviates from the current pixel then the value is reduced linearly. If the threshold cloud top height is 5 km, for example, and the difference between the current pixel and adjacent pixel is 2.5 km, then the value for that adjacent pixel location is 0.5. If the difference reaches 5 km or greater, then the value is 0.0. For same and related cloud type tests, the result is assigned in a binary sense (0.0 or 1.0).

The above procedure is repeated for each similarity test type. After all tests are complete, a final weighted sum is produced using the weights shown in the right column of Table 1. When this procedure has been completed for each previously-evaluated adjacent pixel, the array of weighted sum tests is examined. If any of the weighted sums exceeds a value of 0.5, then the pixel having the maximum value is selected as being the group bearing closest similarity to the test pixel, and the test pixel is assigned to that same group identification number. If none of the weighted sums exceeds 0.5, then the test pixel is deemed unique enough to have its own, new, group number assigned to it.

At the end of the grouping analysis, each cloud pixel will be associated with only one group. A group can be comprised of a single cloud pixel if it is not associated with any other cloudy pixels at initial time. Thus, in the limiting case of total non-similarity among the cloudy pixels, the number of groups can match the total number of cloudy pixels in the scene. After the groups have all been identified, a dominant cloud type, cloud top pressure, mean cloud top height, and maximum optical depth based on the pixel members of each group is determined for tracking purposes. Whereas calculation of surface irradiances is done on a pixel-by-pixel basis, the pixels common to a group will advect together over the forecast period.

An example of this grouping analysis is shown in Fig. 3. The reduction in structure seen in the group analysis reflects the consolidation of many cloudy pixels into contiguous structures, based on the logic described above. The connectivity of some cloud structures may result in rigid-body advection of a large cloud field. Likewise, if a cloud group number changes (as thresholds are surpassed) for a contiguous cloud this can lead to artificial cloud breaks (producing spurious ramps) along the group interfaces during the advection process. The tuning of the group logic to avoid these unrealistic behaviors and artifacts is an ongoing development of *CIRACast*.

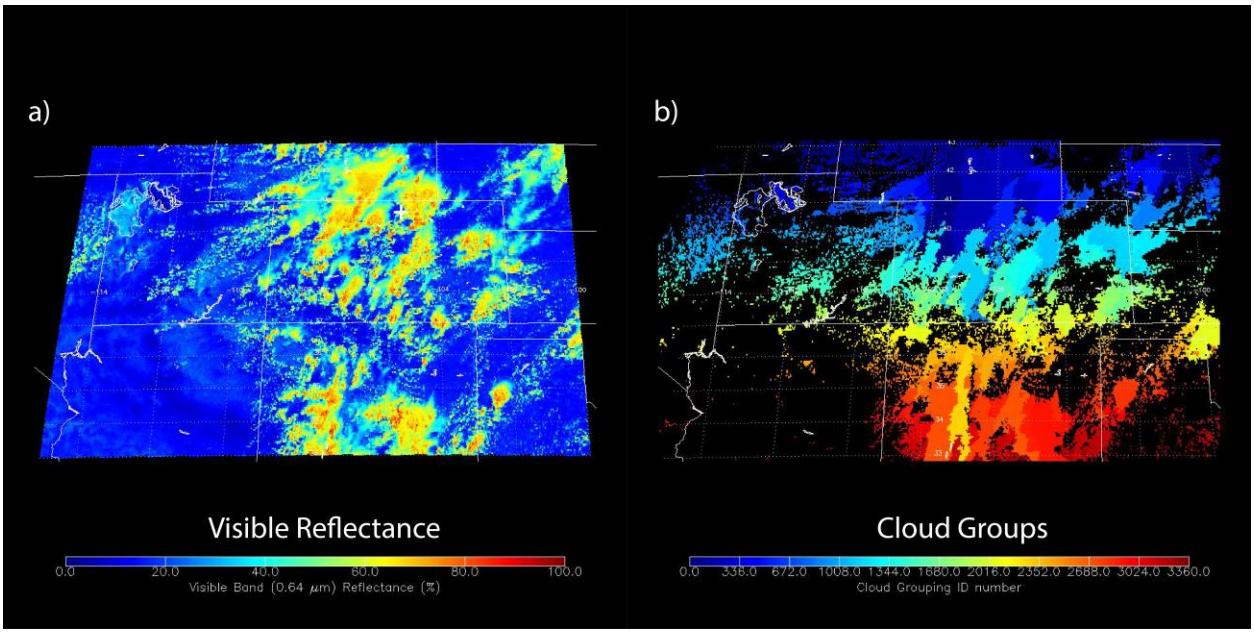

Fig. 3. a) GOES visible reflectance for a convective scene over the southwest U.S. b) Cloud groups identified from this scene, based on the similarity rules described in Section 3.1.

3.2 Cloud Advection

The advection level for winds used to move a given cloud group is currently assumed to be the cloud top height of the group's reference pixel. Once the interpolated wind vector is determined from GFS four-dimensional (space + time) interpolation, it is used to compute a linear displacement of the group's reference pixel location (latitude/longitude, parallax corrected). An updated shadow location (based on the new cloud location and the time-adjusted solar geometry) is computed. To avoid the break-up of a cloud group over time in the presence of a divergent wind field, a reference pixel (one defined for each group) is used to determine these shifts, and the shifts are applied uniformly to all members of the group. Similarly, a dominant cloud height, based the optical-depth-weighted cloud top heights of the group, is used to determine the magnitude of the shadow placement for all the group members.

An important consideration for the advection of cloud groups across a fixed grid is that a group of pixels, once shifted in space by a wind vector, will no longer align perfectly with the original grid. We must therefore have a way of translating the cloud group back to the output grid without losing information about the analog location of the cloud group along the way. The output grid is the same spatial dimension as the initial satellite observation data. The cloud groups are mapped to the output grid at each time step in the advection, while maintaining a record of the groups exact location. Any location where the output grid does not contain a cloudy pixel is treated as a clear-sky pixel for surface irradiance calculations.

The output of the advection code is a stored array of cloud properties retrieved from CLAVR-x whose location latitude and longitude evolve in time. In this way, cloud groups follow streamlines of flow as defined by the model wind field, allowing for representative advection behavior in curved

flows as opposed to linear extrapolation. While new clouds are not formed during the advection, it is possible that some groups may intersect, particularly in cases of strong vertical wind shear (speed and directional). A limiting assumption to the method is that clouds do not evolve significantly over the forecast period. The cloud property arrays as retrieved from CLAVR-x maintain their values; only the locations of the clouds and their shadows are modified.

3.3 Geometric Considerations

The principal goal of short-term solar forecasting is to predict the passage of cloud shadows across the discrete locations of solar farms. The spatial scale of these farms vis-à-vis the resolution of the satellite observations presents a specific challenge, as even a relatively large (e.g., 100 acre) farm occupies only ~40% of a standard 1 km^2 satellite pixel. As satellite imaging radiometers advance in their spatial and temporal resolution, the ability to hone in on scales of relevance to these solar farms increases. However, resolving actual cloud shadows at these scales requires careful account of the satellite and time-evolving solar geometry. This section presents the methodology adopted by *CIRACast* for this purpose.

There are two main considerations for addressing the cloud geometry problem: satellite viewer parallax and the casting of shadows. Unless a cloud is viewed from directly overhead, its geolocation (i.e., projecting its sub-cloud location onto the ellipsoid) will include parallax displacement that is a function of the cloud's height above the surface and the obliquity of the viewer angle—larger values for each quantity will result in larger displacements. The direction of displacement is always away from the observer, such that corrections for parallax shift the locations of clouds *toward* the sub-satellite (nadir) point along a great circle arc that connects the satellite-sub-point to the apparent location of the cloud. Likewise, the shadow cast by this cloud will not reside at the sub-cloud point on the surface unless the sun is directly overhead. The shadow cast by the cloud is in the direction away from the sun in a way that is tied to the cloud height and the solar geometry.

First, the height of the cloud must be computed to determine the correct solar geometry for the casting of shadows by cloud features. Secondly, using the derived cloud-top information, the correct location of cloudy pixels over the surface must be calculated to correct for parallax effects from the viewing perspective of the satellite. Finally, detailed information about terrain elevation is required to compute the location on the surface where shadows are intercepted by terrain. Corrections for satellite viewing parallax were based on a method described in Vicente et al. (2002) application to an ellipsoidal Earth. Owing to typographical errors in some of the key equations of Vicente et al. (2002), and the significance of this work to the current application, we have updated the salient elements of that derivation. These details are included in Appendix 1 of this paper.

Once the sub-cloud location has been determined from the parallax correction, using the CLAVR-x retrieved cloud top height and satellite viewing geometry, a subsequent calculation based on the new location, cloud top height, and *solar geometry* is made to 'cast' the cloud shadow down to the surface along the direction of the solar direct beam. The procedure follows identically to that of the parallax correction described in Appendix A, but operates from the perspective of the sun and is applied in the reverse direction as explained here. We begin by using the parallax-corrected

cloud location as original location $(X,Y,Z)_{cld,app}$ in Eqs. A.3-A.5, and substitute the sun's position (i.e., the time-dependent sub-solar latitude and longitude, calculated from solar geometry software) for $(X,Y,Z)_{sat}$ for the satellite position in Eqs. A.6-A.8. We then utilize the satellite-retrieved cloud height (H_{cld}) as before to determine a 'parallax corrected location' (Eqs. A.18-A.22) which assumes that the sun is the "viewer" in this case. A range and azimuth from the original location to this corrected location is computed using spherical geometry software. To cast the shadow, the azimuth is rotated 180° (the opposite direction of the computed parallax correction) and a distance defined by the computed range is traversed from the original parallax-corrected cloud location to arrive at the $(\theta_{shad}, \phi_{shad})$ location of the shadow.

As a minor modification to account for shadows cast upon elevated terrain, H_{cld} is adjusted in the above equations by subtracting from it the surface elevation defined at the parallax-corrected cloud location (from the USGS Global 30 Arc-second Elevation model, GTOPO30; https://lta.cr.usgs.gov/GTOPO30). In this way, a shorter range of shadow adjustment would be computed for a cloud of given height located over high-elevation terrain vs. a location at mean sea level. The implicit assumption is that the surface elevation at the derived shadow location is equal to that at the sub-cloud location. This assumption breaks down in highly variable terrain (e.g., a shadow cast onto a mountain side or into a valley), and would require iterative corrections to account for the elevation differences between the sub-cloud and shadow locations. For the current application of *CIRACast* to solar farms located in non-complex terrain regions, these higher-order adjustments to shadow placement are ignored.

The downwelling solar irradiance values for each of the cloudy pixels comprising the cloud group are assigned to the shadow-cast locations. These parallax correction and shadow-casting calculations are computed at each time step in the time series output from the *CIRACast* advection algorithm per the flow diagram shown in Fig. 2.

4. *CIRACast* Examples

4.1 Colorado Ramp Forecast

Fig. 4 shows GOES-West visible-band imagery over the Colorado region on 6 March 2013 from 2000 to 2300 UTC (or 2:00 PM to 5:00 PM, Mountain Standard Time). The imagery depicts a north/south oriented upper-level cloud band drifting across the central to eastern part of the state. Toward the end of the time series, and the solar zenith angle increases in the late afternoon, shadows cast by these high clouds can be seen extending to the east across the High Plains of Colorado, far removed from the sub-cloud surface locations.

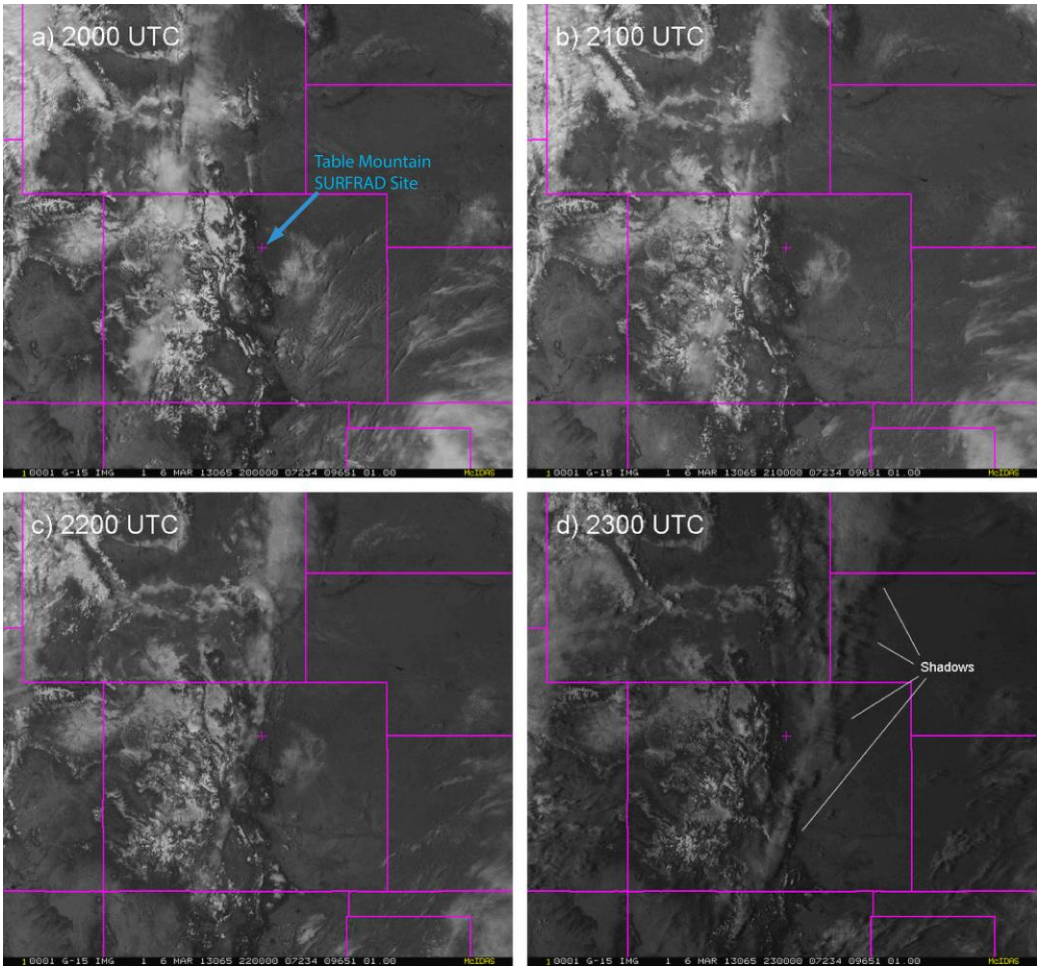

Fig. 4. GOES-W visible reflectance captures a north/south-oriented band of high clouds crossing over the Colorado region on 6 March 2013 at selected times of a) 2000 UTC, b) 2100 UTC, c) 2200 UTC, and d) 2300 UTC. A purple cross denotes the location of the Table Mountain SURFRAD site in Boulder, CO.

The corresponding *CIRACast* predictions of downwelling GHI at the surface are shown in Fig. 5. The forecast captures both the general trend toward lower values of background GHI in the later afternoon and the distribution of enhanced GHI suppression due to cloud shadows. Eastward propagation of these clouds over the afternoon hours produced a series of ramps at the Table Mountain SURFRAD site located in Boulder, Colorado, denoted by a white cross. By inspection of Fig. 5, the cloud layer was predicted to impact this site toward the latter half of the 2100 UTC hour.

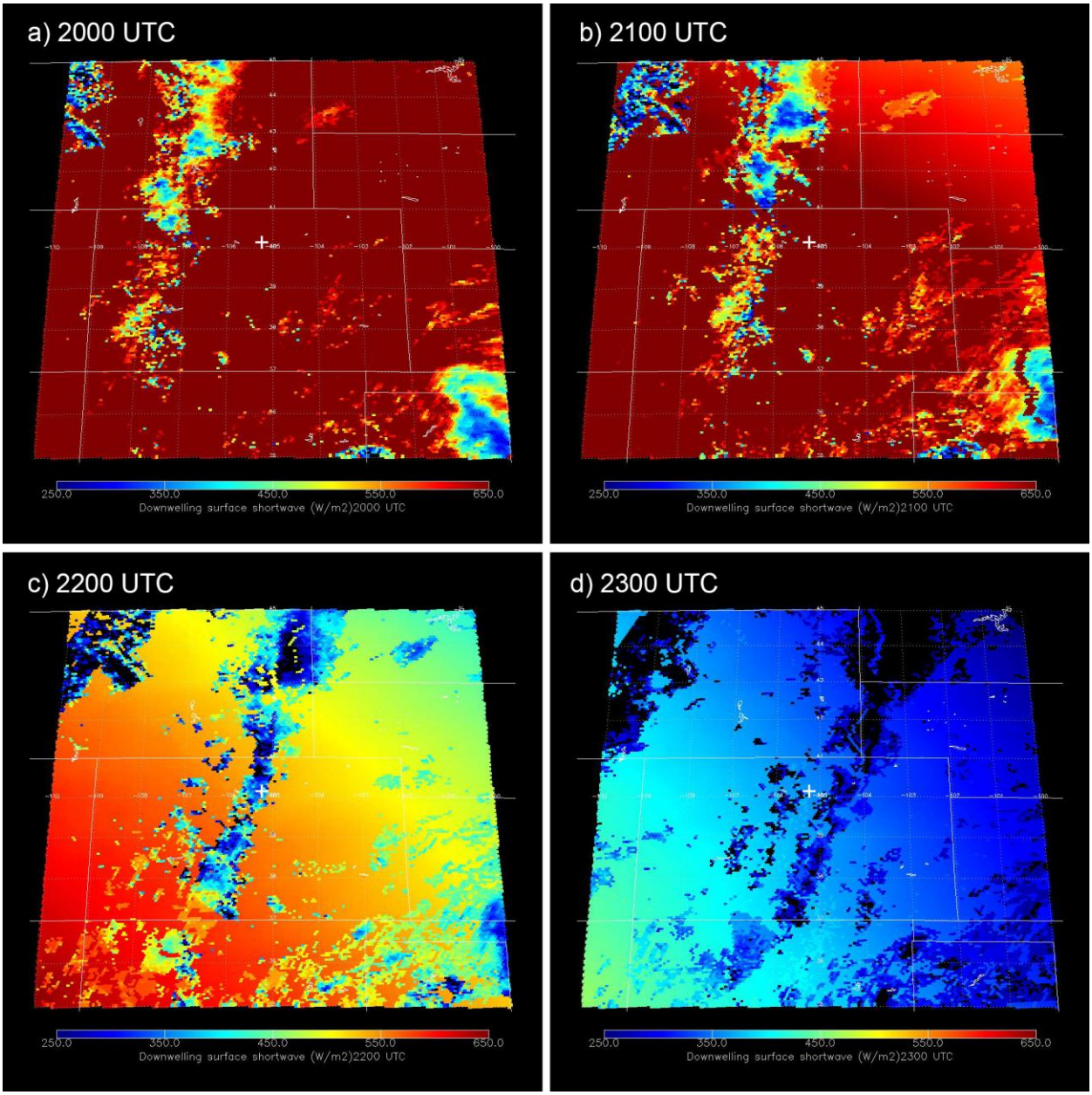

Fig. 5. CIRACast forecasted downwelling GHI (W/m²) at the surface corresponding to Fig. 4. In each panel, a white cross denotes the location of the Table Mountain SURFRAD site in Boulder, CO.

The *CIRACast* predictions are shown along with the Table Mountain SURFRAD observations in Fig. 6. For this case study, CIRACast was initialized at 2000 UTC and run for several hours at 5-min forecast steps. In general, *CIRACast* captures the onset of afternoon ramp activity reasonably well, although differences exist in the specific timing and magnitude of the ramps. The onset of the primary ramping event at approximately 2200 UTC was predicted correctly. However, ramp misses and false alarms were also present, owing to changes in cloud structure (e.g., formation and dissipation) that is unaccounted for by *CIRACast*. Specifically, an observed ramp at approximately 2130 UTC was missed entirely, and two 'false ramps' were predicted during the 2300 UTC hour.

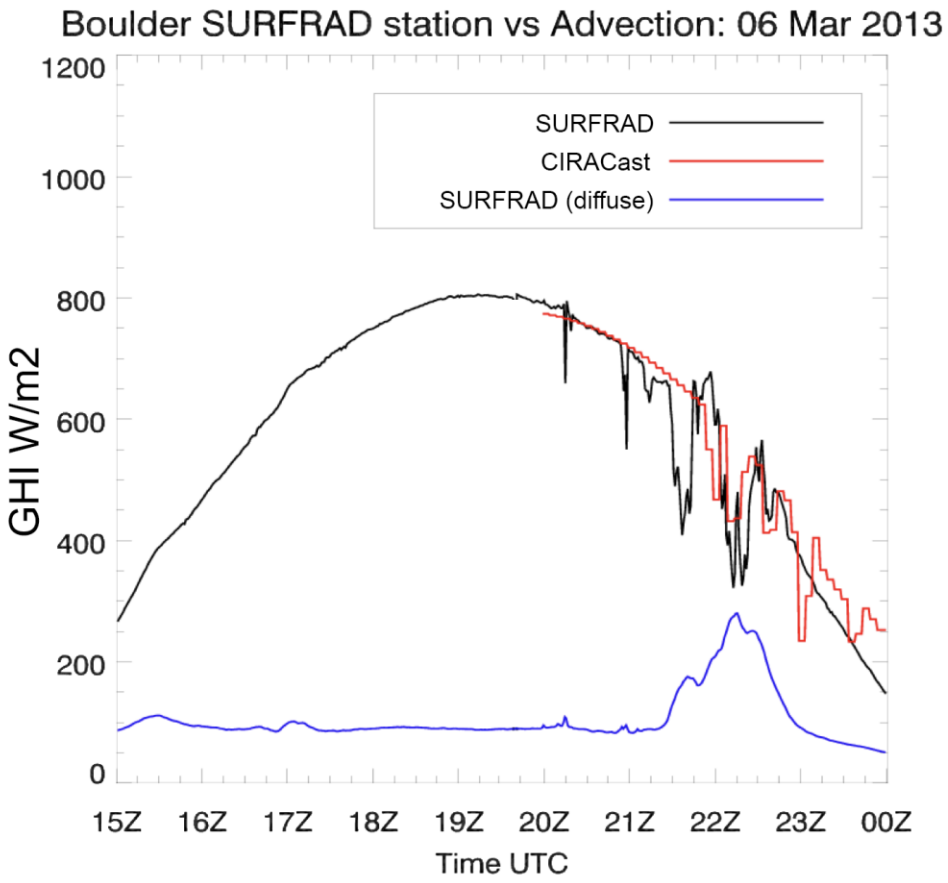

Fig. 6. CIRACast multi-hour solar forecast (initialized at 2000 UTC, 5-min resolution) of GHI at Table Mountain SURFRAD station for the PM cloud case shown in Fig. 3.

4.2 Caveats of Evolving and Stationary Cloud Fields

Since simple cloud advection techniques like *CIRACast* do not consider clouds prognostically like a cloud-resolving NWP model can, there is no account for cloud generation (e.g., due to lifting along a frontal boundary, surface heating), cloud dissipation (e.g., due to dry air entrainment, subsidence, mixing-out of boundary layer fog, etc.), or vertical changes to an existing cloud field which impact shadow properties. These understood limitations contribute to a large portion of the observed error in GHI ramp forecasting. These errors in general will increase with forecast time, as cloud evolution processes begin to dominate the state of the future cloud field. The timescales for decorrelation between the current cloud field (advected by winds) and future cloud distribution are tied closely to the meteorological conditions, local surface properties (including topography), time of day, and season. While this cannot be generalized, location-specific performance statistics can be developed based on local constraints to surface properties and the prevailing weather (climatology) of a given region.

A key issue that was revealed during statistical and case-study validations of *CIRACast* is ramps produced by the false advection of stationary cloud features. For example, orographic clouds in mountainous regions (e.g., the Colorado Front Range) form and dissipate with the ascent and

descent of air parcels forced over the terrain. Likewise, the distribution and evolution of low-level marine stratocumulus (e.g., along coastal California) is governed by terrain blocking, pooling of cool air at night in drainage basins, and inland burn-off during the day. These processes are not accounted for in the advection model. As such, such clouds may be propagated downstream by the prevailing model winds, leading to significant over-forecasting of cloud ramps.

An example of false advection for a marine stratocumulus layer along the California coastline is shown as Fig. 7. Here, marine boundary layer clouds hug the coastline over the course of several hours, while the advection-based GHI forecast (which does not account for terrain blocking and cloud burn-off) proceeds to move the entire cloud field inland per the NWP southerly flow. The advection leads to false GHI ramping predictions at coastal stations.

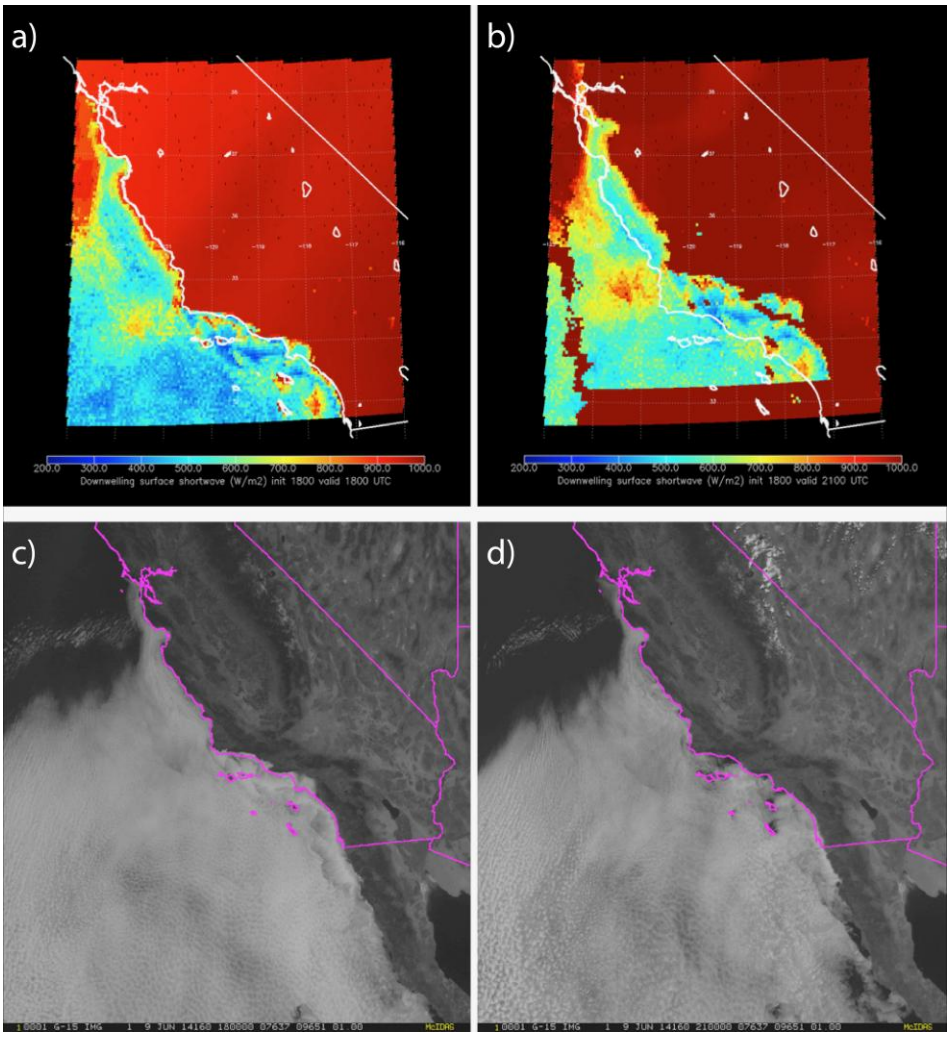

Fig. 7. Example of false inland advection for a marine stratocumulus field off the southern California coast. Upper panels show GHI at a) initial observation time of 1800 UTC, and b) three hours later, having been advected onshore by a southerly model wind field. Lower panels (c) and (d) show GOES-West visible imagery 1800 and 2100 UTC, respectively, confirming that the cloud deck remained offshore over this period.

One way to minimize the errors arising from the scenario shown in Fig. 7 is to account for terrain height vis-à-vis cloud height, and invoke low-level blocking. *CIRACast* is currently being retooled in this way—preventing cloud groups from advection when they abut terrain that exceeds the groups cloud top height. Such logic will fail in the case of orographic clouds, however. Atmospheric motion vectors (AMV) derived from satellite observations (Rabin et al., 2004; Velden and Bedka, 2009) are insufficient for this purpose, as they do not provide a dense vector grid (e.g., at the pixel level of the satellite's spatial resolution) and are not analyzed for stationary targets such as orographic cloud edges. Dense motion vectors derived from optical flow techniques (e.g., Farnebäck, 2003), coupled with a satellite-derived cloud mask, may be more effective in identifying and handling stationary clouds. This is another area of ongoing development for *CIRACast*.

4.3 Preliminary Analysis of Statistical Performance

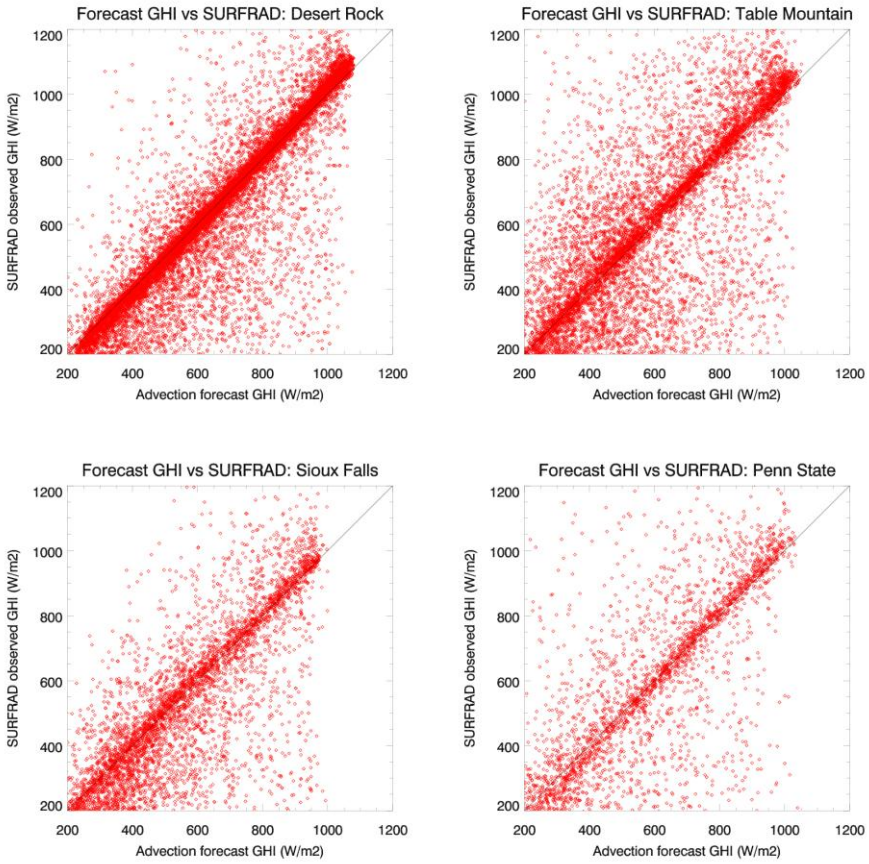

Figure 8. Scatter plots of observed vs. CIRACast-forecasted GHI for four SURFAD sites: Desert Rock, NV, Table Mountain, CO, Sioux Falls, SD, and Penn State, PA. Data compiled over periods between January 2014 and December 2016.

Fig. 8 compares observed and forecasted GHI for selected SURFRAD sites distributed across the U.S. Data shown are for 0-1 hour forecasts compiled for each of the sites over periods between January 2014 and December 2016. The specific procedures used to quantify forecast uncertainty in

solar forecasting systems remains a topic of considerable debate. While efforts to engage utility stakeholders to identify best-practice metrics continue, there remain no universally agreed-upon standards for forecast metrics (Orwig et al. 2015.) Regarding normalized mean absolute error (nMAE, sometimes referred to as 'Mean Absolute Percentage Error', or MAPE), different approaches to the normalization of the error metric have been published. When considering errors measured across the time-varying solar input, many techniques elect to normalize the errors using the clear-sky solar irradiance computed at the validation time (Marquez and Coimbra 2013b, Sangrody et al. 2017) as opposed to using a mean insolation (all-sky) computed over the entire period. These studies suggest that normalizing by the time-varying clear-sky component captures the stochastic variability of solar irradiance. As such, MAE values reported in the current work were normalized by clear-sky GHI values (MAE_{clr}) valid at each measurement time.

Table 2: Forecast Mean-Absolute and Root-Mean Squared Errors for selected SURFRAD stations as a function of forecast window

SURFRAD Site	*MAE (W/m²)*		*MAE_{clr} (%)*		*RMSE (W/m²)*		*RMSE (%)*	
	1hr	*3hr*	*1hr*	*3hr*	*1hr*	*3hr*	*1hr*	*3hr*
Desert Rock, NV	61.9	74.5	8.5	9.6	119.2	141.2	17.8	17.9
Table Mtn, CO	130.1	162.4	17.2	20.6	194.7	237.9	24.9	28.8
Penn State, PA	125.3	185.5	14.7	24.8	194.2	267.7	21.9	34.2
Sioux Falls, SD	109.9	146.3	15.1	20.2	168.5	219.4	11.7	29.1

Overall values of (MAE, MAE_{clr} and RMSE) for 1- and 3-hr forecasts for the SURFRAD sites are presented as Table 2. Forecast error, represented by RMSE, exhibit larger overall errors; this is anticipated due to the nature of ramp forecasting errors, where individual large errors contribute more to the overall error computation than with MAE. Forecast errors for the 1-hr timeframe are lower than those for the 3-hr timeframe for both MAE and RMSE by ~20-40%, demonstrating the fall-off in skill of advection-only based forecasts, which neglect cloud evolution and formation/dissipation during the forecast period.

As a comparison to these results, MAE values for 1-hr forecasts for the Desert Rock site were also computed by Perez et al. (2016; hereafter, referred to as "P16") using a calculation of MAE that is indexed to the observed (i.e., not clear-sky) GHI. For hour-ahead forecasts on a 0.1x0.1-degree grid (~11 km), NWP forecasts demonstrated MAE values of 20.8% (the NOAA High-Resolution Rapid Refresh (HRRR) model), 11.0% (European Centre for Medium-Range Weather Forecasts (ECMWF) model), and 10.6% (GFS), while the P16 SolarAnywhere Version 4 commercial product demonstrated errors of 8.4% at the ~11 km grid resolution. It is important to note that due to differences in the spatial resolution (~4 km *CIRACast* vs. 11 km in P16) and GHI normalization of MAE (clear-sky in CIRACast vs. observed in P16), the comparison between the two methods is not direct. Higher spatial resolution will drive up the *CIRACast* MAE compared to P16. while clear-sky normalization will lower *CIRACast* MAE compared to P16.

Furthermore, small errors in advection, shadow casting, and optical properties can translate to significant uncertainties at the pixel level, making improvements to smart persistence forecasts very difficult. Despite the understood limitations of the current *CIRACast* method, the MAE

performance was found to be on par with other techniques. For example, for one of the more challenging SURFRAD validation sites (Penn State), the smart persistence MAE was computed as 142.1 W/m^2 (16.0%). Following the form of skill score (SS) from Antonanzas et al. (2016):

$$\frac{\qquad}{\qquad} \quad 100\%, \tag{2}$$

yields an SS of 11.8% in this case. Meanwhile, the Desert Rock site produced smart persistence MAE of 58.1 W/m^2 (7.5%), or an SS of -6.5%. Both values fall in a family ranging from -40 to +40 % based on an ensemble of techniques reported in the literature (Antonanzas et al., 2016). Ostensibly the negative value at Desert Rock would appear to be worse performance, but this is where consideration of what constitutes a meaningful metric comes into play. '*Persistence*' implies no ramp events whatsoever—the GHI scales with the initial atmospheric transmittance and varies with daytime parabolic pattern of downwelling solar irradiance. So, from a total (time integrated) energy standpoint, persistence may win-out in the MAE statistics. However, it will not capture the timing and variability of cloud-induced ramps which are key to solar energy resource management (e.g., load balancing) and energy dispatch in the short-term time horizon.

The magnitude and spread of MAE among the various comparisons speaks to the significant challenges faced by advection techniques in different meteorological regimes. For example, the MAE for Table Mountain was roughly two times larger than Desert Rock. This is almost certainly due to the increased amount and complexity of cloud cover encountered over the Rocky Mountains compared to the desert site. As mentioned previously, the presence of orographic clouds over the Colorado Front Range presents an inherent challenge for techniques that are predicated on cloud advection.

4.4 Sensitivity to Geometry

As described in Section 3.3, *CIRACast* accounts for parallax effect in the satellite view and cloud shadow locations utilizing solar geometry and retrieved cloud top heights. The importance of the parallax correction and proper casting of a cloud's shadow are illustrated in Fig. 9, which shows the horizontal displacement, neglecting topography, caused by both effects as a function of cloud top height and either satellite zenith angle (for parallax) or solar zenith angle (for shadows). The displacement increases with cloud top height, so these corrections are especially significant for cirrus and cumulonimbus clouds. The parallax correction is most significant for higher satellite zenith angles (i.e. when clouds are located closer to the limb of the measurement), while the shadow correction is most significant when the solar zenith angle is high.

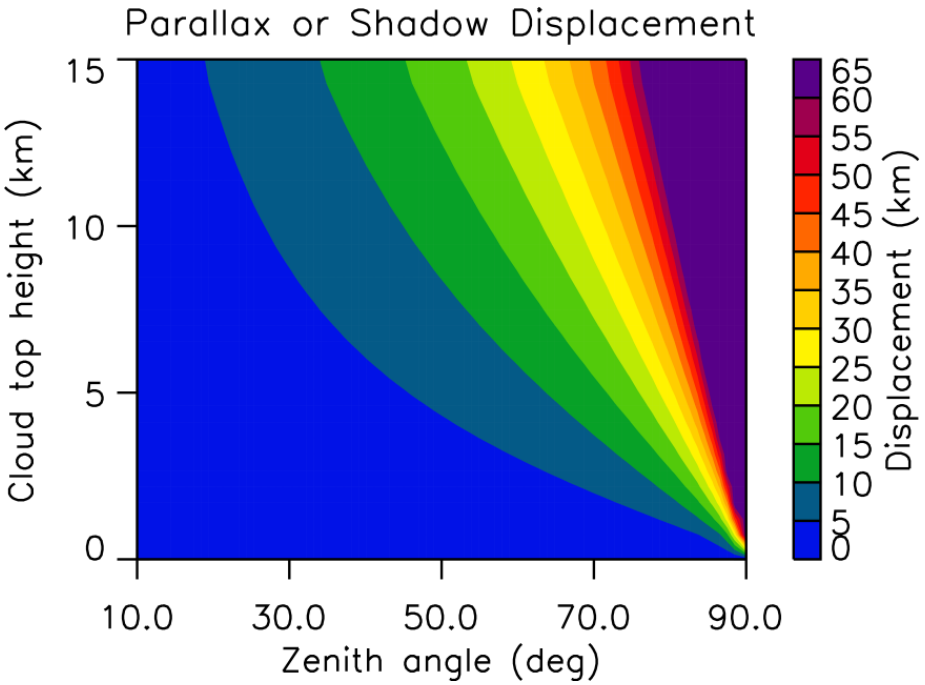

Fig. 9. Horizontal displacement as a function of cloud top height, neglecting topography, between a cloud's nadir location and either (1) its apparent location due to viewer parallax as a function of satellite zenith angle; or (2) the farthest extent of the shadow cast by the cloud as a function of solar zenith angle.

Using case studies, we have analyzed the sensitivity forecast outcomes regarding parallax correction, shadow prediction, and wind interpolation as a function of retrieved cloud height. Fig. 10 demonstrates the impact of the each of these factors relative to a "control" case where all three factors are accounted for. The top panel shows trajectories for two cloud groups over Colorado over the course of three hours. The left (western) group has a cloud top of 11.6 km and is moving northeast, while the right (eastern) group has a cloud top of 6.1 km and is moving southeast. Owing to the height-dependence of parallax shift and shadow casting (Fig. 9), the higher cloud would be expected to produce greater errors, growing with time. This expectation is born out for this example, as seen in the lower panels of Fig. 10. In both cases, removing the shadow correction from the control (blue line) resulted in a maximum error of about 10.5 km for the higher cloud group. The magnitudes of these errors are significant, since displacements of even a few km can alter whether a passing cloud impacts a solar array.

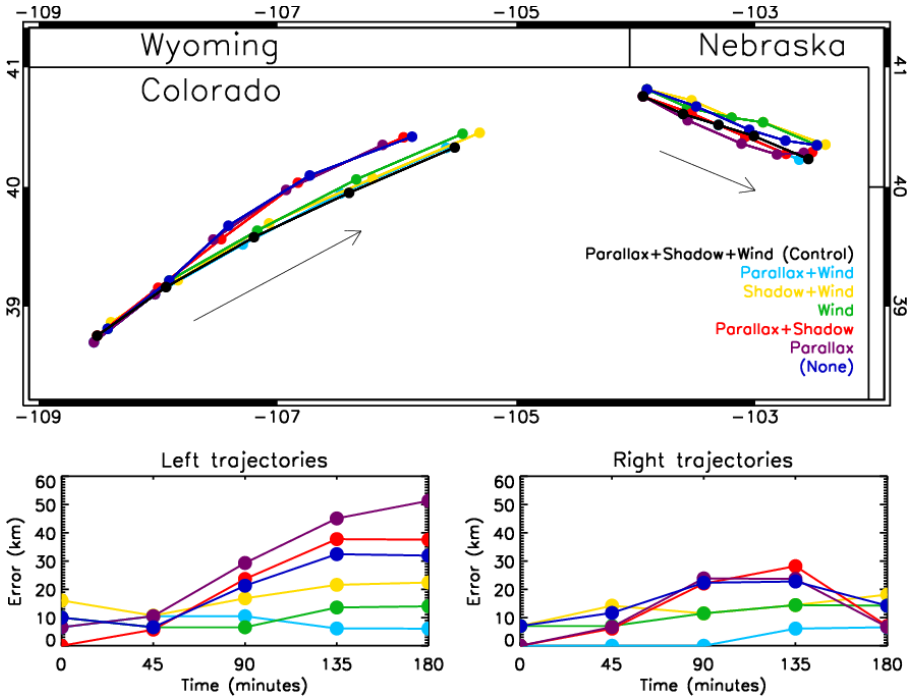

Fig. 10. (Upper Panel): Cloud trajectories computed for two cloud groups on 1 August 2013. Dots indicate tracking feature locations in 45-minute time increments; arrows indicate the general direction of cloud group motion. The colors given in the legend indicate the corrections applied for each case (parallax, shadow location, and updating with interpolated wind vectors). (Lower Panels): position errors relative to the black "control" case for the two sets of trajectories. Cloud top height of the western group is 11.6 km, and of the eastern group is 6.1 km.

Removing the parallax correction from the control (yellow line) is more significant, with errors exceeding 20 km for the higher topped cloud group. In this case, however, the single most important feature is the update to the cloud motion vectors via interpolation of the model wind field. When these updates are removed from the control (red line), the left cloud group drifts approximately 50 km too far to the west over three hours. This growth of error in curved flow environments highlights a benefit of the *CIRACast* NWP-model coupling that cannot be replicated with a feature-tracked vector approach to cloud advection, which moves clouds using wind vectors defined at initial time. The effect is somewhat muted in the right group: errors grow rapidly after 45 minutes as the non-wind corrected cloud group quickly accelerates to the southeast. In the control group, however, the rate of advection has been slowed by the regular updates of the interpolated model wind field, which has slowed relative to the initial wind field. After 135 minutes, wind-related errors in the right group decrease, though this is mostly circumstantial: the cloud group takes a sharp turn to the east, placing it near the final location of the control group, which arrived by a much different path. A more rigorous statistical analysis would likely show a growth in error as a function of time and cloud height.

4.5 Application within Sun4Cast

Surface forecasts of GHI for several SURFRAD locations, using observations from both GOES-East and West, were produced operationally for approximately two years in support of operational demonstrations as part of a Department of Energy SunShot program, led by the National Center for Atmospheric Research (Haupt et al., 2017). As a component of the NCAR *Sun4Cast* model, *CIRACast* was configured to provide 0-3 hr forecasts of GHI at 5-minute time steps over selected locations throughout the U.S. During these *Sun4Cast* demonstrations, *CIRACast* performed at a MAE of ~49 W/m^2 for non-complex cloud regimes, and an upper-bound MAE of ~116 W/m^2 MAE for complex cloud situations. Compared to 'smart persistence' forecasts, where the GHI is predicted using a constant transmittance value derived from current conditions and applied to the clear-sky forecast, the current scheme offered an overall improvement of approximately 6-14 W/m^2 for the range of cases considered.

Lee et al. (2017) consider *CIRACast* in a multi-element (statistical, advection, and NWP) evaluation of *Sun4Cast* forecast skill using a distribution of surface pyranometers operated by the Sacramento Municipal Utility District (SMUD). For this evaluation, they consider four cases (clear, morning time marine stratocumulus, fair weather cumulus, and overcast conditions) to exercise the models under a diverse array of conditions. Their findings point toward areas of improvement for *CIRACast* which are now being implemented. Results indicate a positive bias in clear sky conditions of ~10% which is related to limitations of the SASRAB irradiance model. These biases will be corrected with the substitution of a modified radiative transfer model (Xie et al., 2016), but are of secondary importance to the main *CIRACast* emphasis on the distribution and timing of ramps. An anticipated issue with the motion of stationary (fog) clouds was confirmed (e.g., Fig. 7), and this will be addressed via a hybrid of feature-tracking derived advection vectors and model wind fusion. In cases of widespread broken and overcast conditions, *CIRACast* captured the observed variability but with a positive bias.

5. On Emergent Needs and the Potential of Next-Generation Satellite Observations

High-resolution solar data are of critical importance for increasing the penetration of solar technologies on the power grid. With solar energy becoming a mainstream source of electricity on the grid, there is a growing need for datasets of high resolution and accuracy for all stages of solar projects. These needs relate to policy decisions and technology selection, feasibility and investor commitment, engineering design and system integration and testing for performance, and operations and maintenance. Various studies (Lew et al., 2013; Hummon et al., 2013) have shown how high resolution solar datasets from surface-based measurements and satellites are critical for studies of national importance. Underscoring the importance of high resolution solar datasets, NREL attempts to model 1-minute solar radiation from the hourly solar radiation datasets available from satellites (Hummon et al., 2012).

In addition, the spatial resolution of satellite datasets is critical for estimating solar variability at power plants (Kankiewicz et al., 2010, 2011). Achieving high-penetration of solar energy using large utility scale PV plants requires better understanding of variations that can occur in power production on the order of minutes. High resolution solar radiation datasets from satellite based

methods form the basis for creating the National Solar Radiation Data Base (NSRDB; George et al., 2008; http://maps.nrel.gov/prospector). This dataset, created and distributed by NREL, is arguably the most used solar radiation dataset in the world for renewable energy purposes. It is therefore important that this database be continuously updated with the highest temporal and spatial resolution satellite datasets available to users.

In the early evening of 19 November 2016, NOAA launched the first of its next-generation GOES-R series (comprising four satellites GOES-R/S/T, and U) from Cape Canaveral, Florida. Renamed to GOES-16 two weeks later after its insertion to a temporary geostationary position at 89.5° W, GOES-16 began collecting first-light imagery in January 2017. GOES-16 is slated to take over GOES-East operations (75.2° W) in late 2017. The next member in the series, GOES-S, is scheduled for launch in 2018, and will eventually take over GOES-West operations (137° W) as GOES-17. The GOES-16/17 tandem will complete the transition to an era of advanced imaging radiometer capabilities that stands to revolutionize solar energy source assessment and short to mid-range solar forecasting.

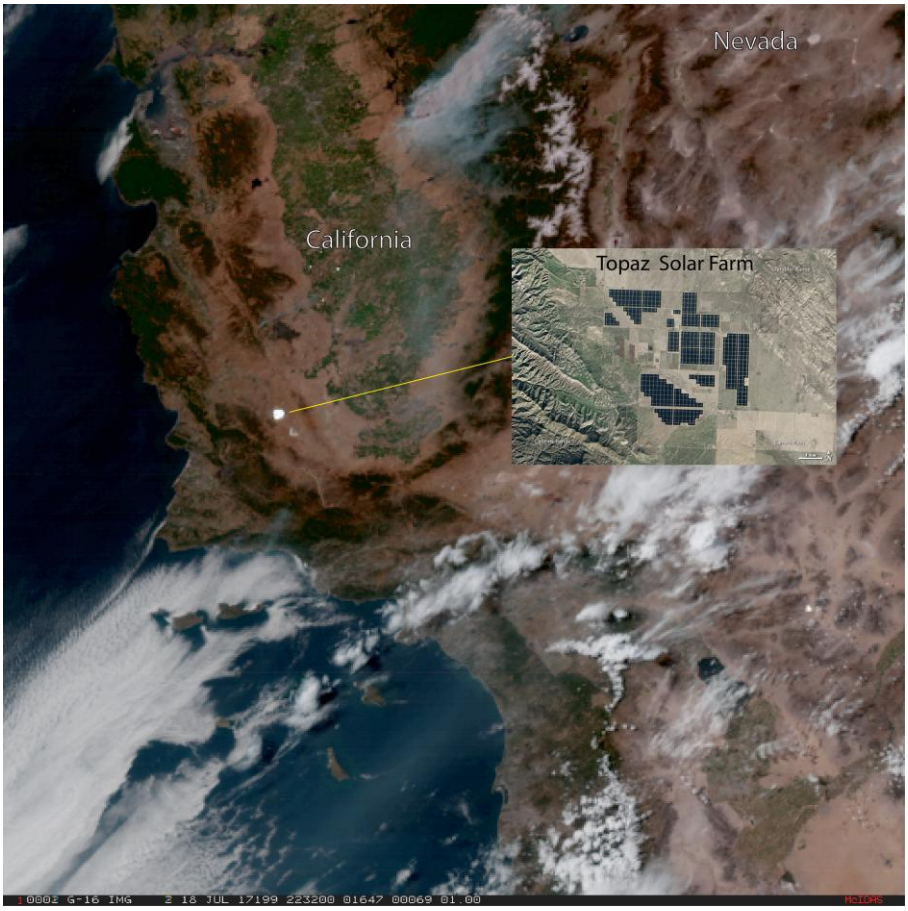

Figure 11. Example of GOES-16 ABI true color imagery over California collected on 18 July 2017 at 2243 UTC (2:43 PM local time). The scale of this image is approximately 1000x1000 km. Reflection of sunlight off the PV panels of the Topaz Solar Farm (inset) accounts for the bright white patch noted in the imagery. (For a ~4-hr animation, see: https://youtu.be/gwXA6XeJvKQ)

The GOES-R class satellites (Schmidt et al., 2017) feature six primary sensors, two designed for earth-viewing and four dedicated to solar and space weather monitoring. The main earth-viewing instrument of interest for solar energy applications is the Advanced Baseline Imager (ABI), an imaging radiometer providing 16 narrowband channels between 0.47 and 13.3 μm in the optical spectrum. Among these bands is a 0.5 km resolution (at nadir) visible band, five additional visible and near-infrared bands at 1 and 2 km resolution, and twelve infrared bands at 2 km resolution. These nominal spatial resolutions degrade with increasing distance from satellite nadir, but the dual GOES-E/W system will maintain these resolutions to within a factor of 2 for the for the CONUS, and will still provide useful information into central Canada and southern Alaska (from GOES-W). In terms of temporal resolution, the default collection schedule (Mode 3, or 'flex mode') provides 15-minute "full disk" (the full field of regard for the satellite), 5-minute Continental United States (CONUS), and two 1-minute mesoscale boxes. The mesoscale boxes can be superimposed and interleaved to provide a 30-second update capability. Compared to the heritage GOES capabilities, the GOES-R series ABI provides 3 times higher spectral resolution, 4 times higher spatial resolution, and 5 times higher temporal resolution, or roughly ~60 times higher total data volume.

An example of the rich spectral and spatial information content present in ABI imagery is shown in Fig. 11 for a region centered on central and southern California, collected on 18 July 2017 at 2232 UTC (or, 2:32 Pacific Daylight Time). The imagery, which is a true color rendering with atmospheric correction based on Miller et al. (2016), captures a complex array of cloud and aerosol features relevant to solar energy, including marine stratocumulus offshore near the Channel Islands, fair weather cumulus clouds in across the inland portions of southern California, and a large plume of smoke from the Detwiler Fire which burned over 80,000 acres of forested land in Mariposa County, CA. The discrete 'bright spot' noted in this image is sunlight reflecting off PV panels at the 550 MW Topaz Solar Farm, in San Luis Obispo County. Being one of largest solar farms in the world at 25 km^2, the Topaz PV array is readily detectable (in this case, for a period of about 1 hr between 2200 and 2300 UTC) by the ABI when the geometry between the sun and GOES-16 aligns along the specular (mirror) reflection angle. Although solar panels are designed to absorb as much sunlight as possible, and reflectance/glare of their solar glass protective coatings are markedly lower (e.g., 5-10%) than standard glass surfaces (e.g., 20-50%, depending on solar incidence angle), the amount of reflected light is more than sufficient for detection. Such an artifact, although transient with time of day and season, could produce spurious ramps in satellite algorithms which equate reflectance with the presence of clouds.

A second example illustrating the potential of ABI high-resolution cloud imagery is shown in Fig. 12 for a portion of southern Texas. As in Fig. 11, the imagery was collected 18 July 2017, but for a slightly later time (2357 UTC). As this region is in the U.S. Central time zone, the local time of the image is 5:57 PM, nearing the time of sunset. Fair weather cumulus clouds orient along the low-level wind flow, forming linear patterns known as cloud streets. Significant biomass smoke (transported from fires in the northwest U.S. and Canada) fills the skies over Dallas, Houston, and regions to the northeast. Meanwhile, in the southwest portion of the scene, a cluster of thunderstorms and associated anvil cirrus cast long shadows (> 60 km) toward the east. Close inspection of the boundary layer cumulus shows similar shadow patterns, with lesser displacements of a few km owing to their smaller vertical extent.

What cannot be captured in any single figure is the inherent advantage of high temporal resolution for the detection and tracking of clouds and aerosol. As mentioned above, ABI provides 5 minute updates over the entire CONUS domain (and higher resolution still, down to 30 s) for limited mesoscale domains. Whereas the mesoscale domains are often moved daily per current needs, the CONUS domain is always available as a baseline for solar energy applications. Examples of the 5 min refresh rate for 18 July imagery used in Figs. 11-12, covering the period 2202-2357 UTC, are provided online (see figure captions for YouTube links). A full CONUS domain loop is also available online (https://youtu.be/kUYo5nJd9Hc), which illustrates the synoptic-scale transport of smoke from the Pacific Northwest to southern Texas, as noted in Fig. 12. These examples were collected from the GOES check-out point of ~89.5° W; GOES-16 will shift eastward by roughly 15°to the operational GOES-E position, yielding western CONUS coverage to GOES-W. GOES-S is scheduled for launch in the early half of 2018. Pending successful commissioning as GOES-17 and after conducting its calibration/validation at the GOES check-out point, it will be migrated to the operational GOES-W position and immediately assume operations—completing NOAA's transition to its next-generation GOES program.

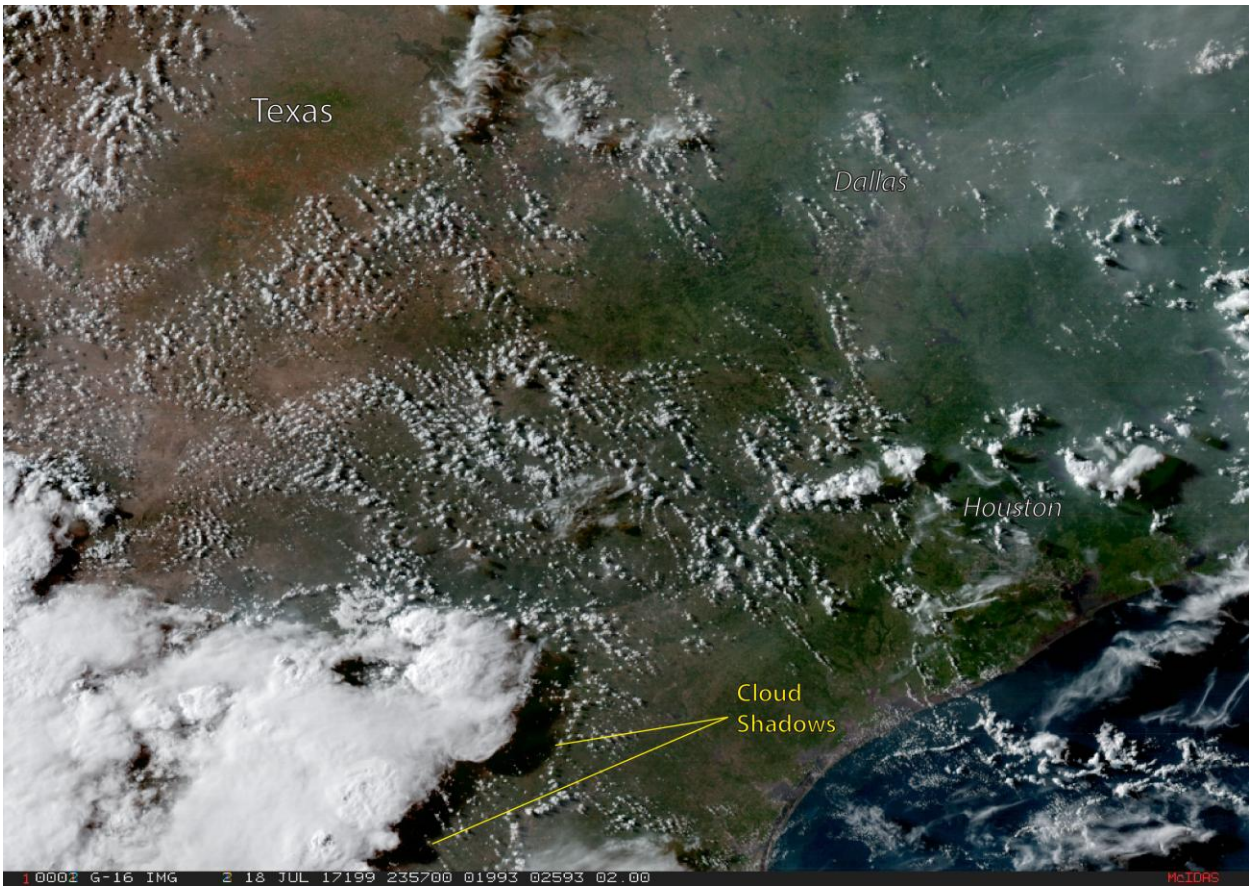

Figure 12. Example of GOES-16 ABI true color imagery over southern Texas collected on 18 July 2017 at 2357 UTC (5:57 PM local time). The scale of this image is approximately 720 x 1020 km. (For a ~4-hr animation, see: https://youtu.be/MUuU0ti9Ctg)

The NOAA CLAVR-x cloud processing software has already been adapted and successfully tested on the pre-operational GOES-16 ABI data stream. The benefits of ABI's improved resolution to the solar forecasting and resource assessment problems are multifold. Its higher spectral resolution provides more accurate retrievals of cloud macro- and microphysical properties used by *CIRACast* for cloud shadow location and surface irradiance estimation. Its higher spatial resolution reduces the effects of sub-pixel heterogeneity which can result in underestimation of cloud height (contributing to shadow misplacement) and various effects on cloud optical properties depending on the underlying background, providing more accurate assessments of solar energy at scales approaching those of the PV farms. The higher temporal resolution allows for more frequent updates, improved cloud motion from feature tracking, and potentially the ability to augment certain limitations of CIRACast via introduction to temporal trends in cloud properties (changes in height and opacity), particularly for short term (< 1 hr) forecasting applications. These observations can be used to complement and extend the three-dimensional cloud information provided by all-sky camera networks, currently used widely by solar energy industry.

6. Conclusion and Future Work

A satellite-based, model fusion technique designed for short term solar irradiance ramp forecasting has been described. The algorithm couples operational geostationary satellite retrievals of cloud microphysical and macrophysical properties to a numerical model, utilizing cloud height information, space/time-varying winds, and solar geometry to advect clouds and locate their shadows on variable terrain. The data are coupled to a solar irradiance model to compute the magnitude of solar irradiance suppression at these shadow locations (or otherwise, the clear sky irradiance). The SURFRAD-validated MAE performance of *CIRACast* for 0-1 hr forecasts, which fell between 8 and 17% depending on location.

A significant limitation for CIRACast, and any cloud advection scheme in general, is the assumption of cloud macro- and microphysical invariance. Throughout the forecast period, clouds are not permitted to grow or dissipate, and no new clouds are formed. The magnitude of errors in the predicted surface radiation field, due to the increasingly unrealistic cloud field over time, is a function of the cloud type and the meteorological regime. The assumption of cloud invariance sets an upper-bound on the skill of advection-based forecasts. Such techniques naturally give give way to NWP models, capable of modifying the cloud field in accordance with the dynamic and thermodynamic processes governing cloud formation, in the intraday timeframe (Diagne et al., 2013). That said, there are some ways to mitigate the limitations of advection schemes and improve their skill beyond the ~1-hr time horizon. These include i) improvements to the cloud grouping logic described in Section 3.1, , ii) analysis of cloud group trends which may provide for short-term evolution prediction, and iii) taking advantage of the higher resolution ABI information as described in Section 5. In that case, the asymptotic behaviors of cloud evolution would need to be constrained as a function of cloud type-dependent statistics and the properties of the atmosphere (e.g., stability, moisture profile, tropopause height). Introducing such approximations to cloud evolution (in the form of empirical, semi-empirical, or physical parameterizations) begins to blur the boundaries between cloud advection and full-physics NWP models.

The SASRAB radiative transfer model currently used by *CIRACast*, has exhibited clear sky bias issues (Xie et al., 2016). Adoption of a more sophisticated radiative transfer code will improve the overall GHI forecast accuracy, especially for statistics which are biased toward the performance under clear sky conditions. In collaboration with NREL, we are adopting the Fast All-sky Radiation Model for Solar Applications (FARMS; Xie et al., 2016) model from NREL, and coupling to it the CLAVR-x retrieved cloud properties. In addition, CLAVR-x provides an estimate of diffuse transmittance (valid over the visible band pass of the ABI). Combining this information with other data that can relate this bandpass transmittance to the broadband shortwave transmittance may provide another fast method for GHI that must be evaluated.

The understood limitations of *CIRACast* help to outline a scope of work for its future development and improvement. Here, we will concentrate on the exploitation of new ABI observations as discussed in Section 5. Despite these pending improvements, the current state of *CIRACast* performance gives cause for optimism that the ceiling of skill has not yet been reached. Adoption of higher resolution NWP models, such as HRRR, would potentially improve the cloud advection in the presence of complex flows. Methods for evaluating forecast performance, including point vs. spatial averaging, instantaneous GHI behavior vs. assessment of variability over defined time windows, and the effects of individual ramps vs. integrated energy must also be revisited in the context of higher space/time satellite observations. In addition, the wealth of satellite-supplied parameters permit detailed examination of forecast error as a function of cloud type and cloud macro/microphysical properties. These represent exciting pathways for advancing our capabilities in this important application of environmental satellites to the outstanding challenges of harnessing the solar energy resource.

7. Acknowledgements

This work was supported by the National Renewable Energy Laboratory [AGJ-040282-01] and the National Oceanic and Atmospheric Administration [NA09OAR4320074#29]. We owe a debt of gratitude to Dr. Daniel T. Lindsey (NOAA/NESDIS) for his assistance in preparing animations of GOES-16 ABI true color imagery, available online.

8. Appendix A: Satellite Viewing Parallax Correction

This Appendix provides updates to a method described in Vicente et al. (2002) for satellite viewing parallax corrections with application to an ellipsoidal Earth. The inputs to the parallax correction calculation are the apparent latitude/longitude $(\theta_{cld}, \phi_{cld})_{app}$ and height (H_{cld}; provided by satellite retrievals) of the cloud, the location of the sub-satellite point $(\theta_{sat}, \phi_{sat})$ and the altitude of the satellite (Z_{sat}). The outputs are the parallax-corrected location $(\theta_{cld}, \phi_{cld})_{pc}$. For a Cartesian coordinate system (X,Y,Z) whose origin is at Earth's center, X-axis intersecting the equator and prime meridian, Y-axis intersecting the north and south poles, Z-axis intersecting the equator at 90° E, the ellipsoidal Earth is approximated as:

(A.1)

Where $R_{E,equat}$ (= 6378.1 km) and $R_{E,pol}$ (= 6356.6 km) are the equatorial and polar radii of the elliptical Earth. The equivalent radius of Earth at the cloud location is given by:

(A.2)

The apparent cloud location $(X,Y,Z)_{cld,app}$ and the satellite location $(X,Y,Z)_{sat}$ are given by:

(A.3)

(A.4)

), (A.5)

and,

(A.6)

(A.7)

), (A.8)

where $R_{sat} = R_{E,equat} + H_{sat}$ (for the geostationary orbit, the satellite altitude H_{sat} = 35786 km).

Recognizing that a line connecting the cloud's apparent position and the satellite position in space will intersect the line connecting the center of Earth to the actual (parallax-corrected) cloud position at the height of the cloud (H_{cld}), and following Eq. A.1, the parallax-corrected location of the cloud $(X,Y,Z)_{cld,pc}$ satisfies:

(A.9)

The apparent and parallax-corrected cloud positions in three-dimensional space are related as:

(A.10)

(A.11)

(A.12)

Inserting Eqs. A.10-A.12 into Eq. A.9, expanding, and solving for *A* via the quadratic equation:

, (A.13)

we identify the following quadratic coefficients:

(A.14)

(A.15)

, (A.16)

where

. (A.17)

Converting back to a latitude/longitude coordinate system, the parallax-corrected latitude is given by:

(A.18)

and the parallax-corrected longitude is given by:

(A.19)

(A.20)

(A.21)

(A.22)

Cloud-top heights used in these calculations were supplied by CLAVR-x, via the algorithm described by Heidinger and Pavolonis (2009). Computed as diagnostic terms are the great-circle distance of the parallax shift (in km), and the azimuth angle of the shift direction (which should always be toward the sub-satellite point).

9. References

Antonanzas, J., Osorio, N., Escobar, R., Urraca, R., Martinez-de-Pison, F.J., Antonanzas-Torres, F., 2016. Review of photovoltaic power forecasting. Solar Energy 136, 78-111. DOI:10.1016.j.solener.2016.06.069

Augustine, J.A., DeLuisi, J.J., Long, C.N., 2000. SURFRAD—A national surface radiation budget network for atmospheric research. Bull. Amer. Met. Soc. 81 (10), 2341-2358.

Augustine, J.A., Hodges, G.B., Cornwall, C.R., Michalsky, J.J., Medina, C.I., 2005. An update on SURFRAD—The GCOS surface radiation budget network for the continental United States. J. Atmos. Oceanic Tech. 22, 1460-1472.

Cano, D., Monget, J.M., Albuisson, M., Guillard, H., Regas, N., Wald, L., 1986. A method for the determination of the global solar radiation from meteorological satellite data. Solar Energy 37, 31-39.

Chow, C.W., et al., 2011. Intra-hour forecasting with a total sky imager at the UC San Diego solar energy testbed. Solar Energy 85 (11), 2881-2893.

Darnell, W.L., Staylor, W.F., Gupta, S.K., Denn, M., 1988. Estimation of surface insolation using sun-synchronous satellite data. J. Climate 1, 820-835.

Dedieu, G., Deschamps, P.Y., Kerr, Y.H., 1987. Satellite estimation of solar irradiance at the surface of the earth and of surface albedo using a physical model applied to Meteosat data. J. Climate Appl. Meteor. 26, 79-87.

Diagne, H.M., David, M., Lauret, P., Boland, J., Schmitz, N., 2013. Review of solar irradiance forecasting methods and a proposition for small-scale insular grids. Renew. Sust. Energy Rev. 27, Elsevier, 65-76.

Diak, G.R., Gautier, C., 1983. Improvements to a simple physical model for estimating insolation from GOES data. J. Appl. Meteor. Clim. 22, 505-508.

Farnebäck, G., 2003. Two-frame motion estimation based on polynomial expansion. Proc. 13th Scandinavian Conf. on Image Analysis, Halmstad, Sweden, 29 June – 2 July, pp. 363-370. ISBN:3-540-40601-8.

Gautier, C., Diak, G., Masse, S., 1980. A simple physical model to estimate incident solar radiation at the surface from GOES satellite data. J. Appl. Meteorology 19, 1005-1012.

George, R., Wilcox, S., Anderberg, M., 2008. National Solar Radiation Database (NSRDB) -10 km Gridded Hourly Solar Database. Solar Resource Assessment Workshop, NREL (National Renewable Energy Laboratory), 38 pp., NREL Report No. PR-550-44443. http://www.nrel.gov/docs/gen/fy09/44443.pdf.

Haupt, S. E., et al., 2017. Building the Sun4Cast System: Improvements in Solar Power Forecasting. Bull. Amer. Meteor. Soc., doi:10.1175/BMS-D-16-0221.1, in press.

Heidinger, A.K., Pavolonis, M.J., 2009. Gazing at cirrus clouds for 25 years through a split window, Part 1: Methodology. J. Appl. Meteor. Clim. 48 (6), 1100-1116.

Heidinger, A.K., Evan, A.T., Foster, M.J., Walther, A., 2012. A naive Bayesian cloud-detection scheme derived from CALIPSO and applied within PATMOS-x. J. Appl. Meteor. Clim. 51 (6), 1129–1144.

Heidinger, A.K., Straka, III, W.C., Molling, C.C., Sullivan, J.T., Wu, X., 2010. Deriving an inter-sensor consistent calibration for the AVHRR solar reflectance data record. Int. J. Rem. Sens. 31 (24), 6493-6517.

Hummon, M., Ibanez, E., Brinkman, G., Lew, D., 2012. Sub-Hour Solar Data for Power System Modeling from Static Spatial Variability Analysis. NREL Report No. CP-6A20-56204, 9 pp. http://www.nrel.gov/docs/fy13osti/56204.pdf.

Hummon, M., Weekley, A., Searight, K., Clark, K., 2013. Downscaling Solar Power Output to 4-Seconds for Use in Integration Studies. NREL Report No. PR-6A20-60336, 24 pp. http://www.nrel.gov/docs/fy14osti/60336.pdf.

Inman, R.H., Pedro, H.T.C., Coimbra, C.F.M., 2013. Solar forecasting methods for renewable energy integration. Progress in Energy and Combustion Science 39, Elsevier, 535-576.

Kankiewicz, A., Sengupta, M., Li, J.Y., 2011. Cloud Meteorology and Utility-Scale PV Variability. Proc. 40th ASES National Solar Conference (Solar 2011), 17-20 May, Raleigh, North Carolina. Boulder, CO: American Solar Energy Society (ASES) pp. 331-333; NREL Report No. CP-5500-55071.

Kankiewicz, A., Sengupta, M., Moon, D., 2010. Observed Impacts of Transient Clouds on Utility-Scale PV Fields. Campbell-Howe, R., ed. Proc. Solar 2010 Conf., 19-21 May 2010, Phoenix, Arizona (DVD-ROM).

Kleissl, J., Harper, J., Dominguez, A., 2010. A Solar Resource Measurement Network for Solar Intermittency at High Spatio-Temporal Resolution. Proc. ASES Annual Conf., Phoenix, AZ.

Lee, J. A., S. E. Haupt, P. A. Jimenez, M. A. Rogers, S. D. Miller, and T. C. McCandless, 2017: Solar energy nowcasting case studies near Sacramento. J. Appl. Meteorol., 56, 85-108.

Lew, D., et al., 2013. Western Wind and Solar Integration Study Phase 2. 244 pp.; NREL Report No. TP-5500-55588. http://www.nrel.gov/docs/fy13osti/55588.pdf.

Marquez, R. and C.F.M. Coimbra, 2013b. Proposed Metric for Evaluation of Solar Forecasting Models. J. Solar Energy Engineering, **135**, 011016-1-9

Miller, S.D., Heidinger, A.K., Sengupta, M., 2013. Physcially-Based Satellite Methods. In Solar Energy Forecasting and Resource Assessment, 1st Edition, Chap. 3. Elsevier, J. Kleissl, (Ed). 462 pp.

Miller, S.D., et al., 2014. Estimating three-dimensional cloud structure from statistically blended active and passive sensor observations. J. Appl. Meteor. Clim. 53 (2), 437-455.

Miller, S.D., et al., 2016. A sight for sore eyes: The return of true color imagery to geostationary satellites. Bull. Amer. Meteor. Soc. 97 (10), 1803-1816,

Orwig, K.D., M.L. Ahlstrom, V. Banunarayanan, J. Sharp, J.M. Wiczak, J. Freedman, S.E. Haupt, J. Cline, O. Bartholomy, H.F. Hamann, B-M Hodge, C. Finley, D. Nakafuji, J.L. Peterson, D. Maggio, and M. Marquis, 2015. IEEE Trans. On Sust. Energy, **6** no. 3, 924-933

Pavolonis, M.J., Heidinger, A.K., Uttal, T., 2005. Daytime global cloud typing from AVHRR and VIIRS: Algorithm description, validation, and comparisons. J. Appl. Meteor. 44 (6), 804-826.

Perez, R., David, M., et al., 2016. Spatial and Temporal Variability of Solar Energy. Foundations and Trends in Renewable Energy, 1(1), 1-44. DOI:10.1561/2700000006.

Perez, R., J. Schlemmer, K. Hemker Jr., S. Kivalov, A. Kankiewicz, and J. Dise, 2016. Solar Energy Forecast Validation for Extended Areas and Economic Impact of Forecast Accuracy. Proceedings, 43rd IEEE PV Specialists Conference, Portland, OR

Perez, R., Ineichen, P., et al., 2002. A new operational model for satellite-derived irradiances: description and validation, *Solar Energy*, 73(5), 307-317.

Pinker, R.T., Laszlo, I., 1992. Modeling surface solar irradiance for satellite applications on a global scale. J. Appl. Meteor. 11, 194-211.

Pinker, R.T., Frouin, R., Li, Z., 1995. A review of satellite methods to derive surface shortwave irradiance. Rem. Sens. Env. 51, 108-124.

Pinker, R.T., Laszlo, I., Tarpley, J.D., Mitchell, K., 2000. Geostationary satellite products for surface energy balance models. COSPAR 2000, 16-23, July, Warsaw, Poland, 2000.

Polo, J., Zarzalejo, L.F., Ramirez, L., 2008. Solar Radiation Derived from Satellite Images. Chapter 18: Modeling Solar Radiation at the Earth's Surface: Recent Advances. Springer, V. Badescu (Ed). 516 pp. ISBN 978-3-540-77454-9.

Rabin, R., Corfidi, A., Brunner, J., Hane, C., 2004. Detecting winds aloft from water vapour satellite imagery in the vicinity of storms. Weather 59, 251-257.

Sangrody, H., M. Sarailoo, N. Zhou, N. Tran, M. Motalleb, and E. Foruzan, 2017: Weather forecasting error in solar energy forecasting. IET Renew. Power. Gener., 2017 **11** 1274-1280

Schmidt, T. J., Griffith, P., Gunshor, M.M., Daniels, J.M., Goodman, S. J., Lebair, W.J., 2017. A closer look at the ABI on the GOES-R series. Bull. Amer. Meteor. Soc. 98, 681-698.

Sengupta, M., et al., 2015. Best Practices Handbook for the Collection and Use of Solar Resource Data for Solar Energy Applications. 255 pp.; NREL Report No. TP-5D00-63112, http://www.nrel.gov/docs/fy15osti/63112.pdf.

Schmetz, J., 1989. Toward a surface radiation climatology: retrieval of downward irradiances from satellites. Atmos. Res. 23, 287-321.

Tarpley, J.D., 1979. Estimating incident solar radiation at the surface from geostationary satellite data. J. Appl. Meteor. 18, 1172.

Velden, C.S., Bedka, K.M., 2009. Identifying the uncertainty in determining satellite-derived atmospheric motion vector height attribution. J. Appl. Meteor. 48, 450-463.

Vicente, G.A., Davenport, J.C., Scofield, R.A., 2002. The role of orographic and parallax corrections on real time high resolution satellite rainfall rate distribution. Int. J. Rem. Sensing 23 (2), 221-230.

Vonder Haar, T., Raschke, E., Bandeen, W., Pasternak, M., 1973. Measurements of solar energy reflected by the earth and atmosphere from meteorological satellites. Solar Energy 14, 175-184.

Walther, A., Heidinger, A.K., 2012. Implementation of the Daytime Cloud Optical and Microphysical Properties algorithm (DCOMP) in PATMOS-x. J. Appl. Meteor. Clim. 51 (7), 1371–1390.

Xie, Y., Sengupta, M., Dudhia, J., 2016. A Fast All-sky Radiation Model for Solar applications (FARMS): Algorithm and performance evaluation. Solar Energy 135, 435-445.

Zelenka, A., Perez, R., Seals, R. and Renné, D., 1999. Effective Accuracy of Satellite-derived irradiance. Theoretical and Applied Climatology 62, 199-207.